ADVANCED FUNCTIONAL MATERIALS
www.afm-journal.de

Molecular Doping of 2D Indium Selenide for Ultrahigh Performance and Low-Power Consumption Broadband Photodetectors

*Ye Wang, Hanlin Wang, Sai Manoj Gali, Nicholas Turetta, Yifan Yao, Can Wang, Yusheng Chen, David Beljonne, and Paolo Samorì**

Two-dimensional (2D) photodetecting materials have shown superior performances over traditional materials (e.g., silicon, perylenes), which demonstrate low responsivity (R) (<1 AW^{-1}), external quantum efficiency (EQE) (<100%), and limited detection bandwidth. Recently, 2D indium selenide (InSe) emerged as high-performance active material in field-effect transistors and photodetectors, whose fabrication required expensive and complex techniques. Here, it is shown for the first time how molecular functionalization with a common surfactant molecule (didodecyldimethylammonium bromide) (DDAB) represents a powerful strategy to boost the (opto) electronic performances of InSe yielding major performance enhancements in phototransistors, Schottky junctions, and van der Waals heterostructures via a lithography-compatible fabrication route. The functionalization can controllably dope and heal vacancies in InSe, resulting in ultrahigh field-effect mobility (10^3 cm^2 V^{-1} s^{-1}) and photoresponsivity (10^6 A W^{-1}), breaking the record of non-graphene-contacted 2D photodetectors. The strategy towards the molecular doping of 2D photodetecting materials is efficient, practical, up-scalable, and operable with ultra-low power input, ultimately paving the way to next-generation 2D opto-electronics.

1. Introduction

Photodetectors capable of sensing light from ultraviolet (UV) to infrared (IR) have become key devices in a broad range of technologies comprising optical sensing, image recognition, motion detection, remote control, biomedical imaging, etc.[1–4] 2D materials have been extensively studied during the last decade as promising photodetecting materials owing to their fast response, high responsivity, photodetectivity, and broad wavelength detection. The wide selection of materials with tunable bandgap obtained by altering the layer numbers and the simple formation of van der Waals (vdW) heterostructures enabled to reach high responsivity (≈10^6–10^7 AW^{-1}), high detectivity (D^*) (≈10^{10}–10^{13} Jones), and ultrafast photoresponse (on the µs timescale).[1,5–12] However, the operation of these high-performance devices requires high bias voltage yielding large power consumption. Such an issue represents a strong handicap for various technological applications such as photosensor in an extreme environment, bio-medical imaging, portable devices, etc. 2D indium selenide (InSe) has recently attracted a great attention because of its ultrasensitive photodetection characteristics outperforming common 2D semiconducting materials such as MoS_2 and WSe_2.[5,6,8,13–16] Such high performances were achieved by means of complex and specific techniques such as ion implantation and nanopatterning, which unfortunately drastically increase the fabrication costs.[6,7,17] A powerful route for tuning physical and chemical properties of 2D materials, which has been thoroughly applied to graphene, TMDs, and BP, consists in molecular functionalization via covalent and non-covalent strategies, resulting in doping, defect healing, increase in bio-compatibility, etc.[18,19] Surprisingly, such an approach has not yet been attempted with InSe for obtaining high-performance devices. Moreover, despite the high electron mobility of InSe, little effort has been devoted to combining InSe with other 2D materials to generate highly responsive p-n photodetectors. This urges us to find viable strategies for the construction of high-performance photodetectors based on InSe and InSe-based p-n junctions.

Here we show how the functionalization with a common surfactant molecule represents a powerful strategy to boost the (opto)electronic performances of 10–15 nm thick InSe flakes exfoliated from commercial crystals yielding to major property enhancements in InSe based phototransistor, lateral Schottky junction, and BP-InSe vdW p-n heterostructures. For the first time we have also fabricated high-responsivity, fast response, low power input 2D photodetectors through a lithography-compatible route in which the performances are enhanced via the functionalization with organic molecules.

Y. Wang, Dr. H. Wang, N. Turetta, Dr. Y. Yao, Dr. C. Wang, Y. Chen, Prof. P. Samorì
University of Strasbourg
CNRS
ISIS UMR 7006, 8 Allée Gaspard Monge, Strasbourg F-67000, France
E-mail: samori@unistra.fr
Dr. S. M. Gali, Prof. D. Beljonne
Laboratory for Chemistry of Novel Materials
Université de Mons
Place du Parc 20, Mons 7000, Belgium
The ORCID identification number(s) for the author(s) of this article can be found under https://doi.org/10.1002/adfm.202103353.

DOI: 10.1002/adfm.202103353

2. Dielectric Engineering InSe Field-Effect Transistor

In order to cast light onto the role of the dielectric characteristics of the substrate, as-exfoliated flakes were transferred onto both Si/SiO_2 and polymer-coated Si/SiO_2 substrate. **Figure 1**a displays the transfer (V_g-I_{ds}) curve of InSe on SiO_2. It reveals modest transport performances with electron mobilities around 0.01 $cm^2\ V^{-1}\ s^{-1}$, being considerably lower than other 2D semiconductors. Such low performances can be ascribed to the abundance of charge traps at the $InSe/SiO_2$ interface which is detrimental to photodetection, also limiting the use of as-prepared InSe as a platform for molecular functionalization, because the leakage current would have a similar magnitude of the drain-source current, yielding device instability.[20,21] Therefore, it is imperative to improve the local environment where InSe is embedded, and in particular its dielectric characteristics. Towards this end, divinyltetramethyl disiloxanebis(benzocyclobutene) (BCB) was chosen as a trap-free dielectric polymer for its easy processability, high thermal and chemical resistance, being an optimal choice for microfabrication of 2D materials.[22] The precursor-free solution-processable and lithography-friendly characteristics made BCB much more advantageous compared to other trap-free dielectrics such as poly(methyl methacrylate) (PMMA, highly soluble in common solvents), polyimide (PI, usually precursor-involved), and hexagonal boron nitride (h-BN, very costly for both CVD-grown and exfoliated materials). The hysteresis of transfer curves has been largely decreased by 30V compared to pure SiO_2 supported devices (Figure S1a, Supporting Information). The top-contact device architecture is depicted in Figure 1b. The resulting capacitance of the in-series capacitor drops from 12.7 nF cm^{-2} for SiO_2 to 6.05 nF cm^{-2} for BCB. As shown in Figure 1a, the 2D conductivity (σ) of InSe drastically increases in devices from (1.99 ± 0.966) × 10^{-4} µS on SiO_2 to 25.30 ± 11.19 µS on BCB, with turn-on voltage fixed around 0V, thereby indicating the unchanged degree of doping on different dielectrics. Similarly, the field-effect mobility of InSe undergoes a major increase from a max value of 0.0116 $cm^2\ V^{-1}\ s^{-1}$ on SiO_2 to 688.2 $cm^2\ V^{-1}\ s^{-1}$ on BCB. The mechanism could be explained through Figure 1c where large defect densities (e.g., point defect P_b center) are formed during the thermal oxidation of silicon, in addition to the polarized surface optical (SO) phonon modes in Si—O bond

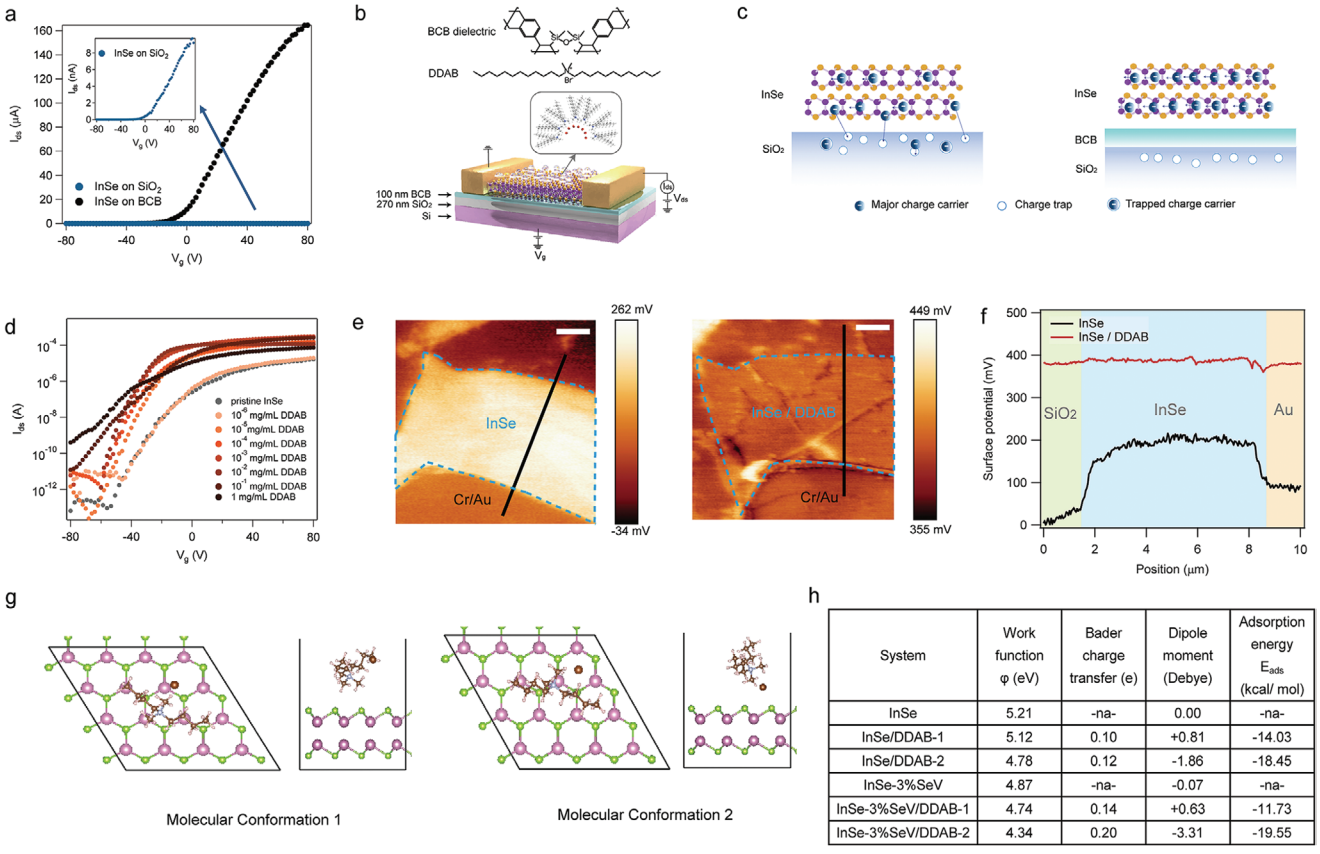

h

System	Work function φ (eV)	Bader charge transfer (e)	Dipole moment (Debye)	Adsorption energy E_{ads} (kcal/ mol)
InSe	5.21	-na-	0.00	-na-
InSe/DDAB-1	5.12	0.10	+0.81	-14.03
InSe/DDAB-2	4.78	0.12	-1.86	-18.45
InSe-3%SeV	4.87	-na-	-0.07	-na-
InSe-3%SeV/DDAB-1	4.74	0.14	+0.63	-11.73
InSe-3%SeV/DDAB-2	4.34	0.20	-3.31	-19.55

Figure 1. Dielectric engineering and molecular doping of InSe FET. a) Comparison of transfer (V_g-I_{ds}) curve of InSe FET onto SiO_2 and BCB. The inset shows the zoom of the transfer curve on SiO_2. b) Illustration of device structure and the chemical structure of BCB polymer and DDAB molecule used in this work. c) Scheme of the mechanism of charge transport enhancement of InSe on SiO_2 and BCB. d) Transfer (V_g-I_{ds}) curve of InSe FET functionalized with DDAB with different concentrations. e) Surface potential measured by KPFM of a few-layer InSe of before and after functionalization with DDAB (scale bar: 3 µm). f) The corresponding line potential profile of marked in black line in (e). The flake is grounded by a Cr/Au electrode during the measurement g) Schematic representation of DDAB physisorbed onto InSe in conformation 1 and conformation 2. h) Summary of DFT calculated work function, Bader charge transfer, molecular dipole moment and adsorption energy of InSe and defective InSe functionalized with DDAB. The smaller work function shift of the experimental value is attributed to the inevitable p-doping to InSe from the water and oxygen in air during the measurement.

oscillatory motions, limiting the mobility of electron transport by introducing localized states and participating in Coulomb scattering.[23–26] By using BCB as a gate dielectric, the interface trap density D_{it} between InSe and the dielectric has decreased by one order of magnitude, leading to a more effective screening of Coulomb scattering, thus increasing the charge carrier mobility and channel conductance.

3. Ionic Molecular Doping of InSe Field Effect Transistor

Although the use of BCB dielectric largely improves the channel conductivity of InSe, the device is in OFF state at $V_g = 0$ V. This raises a major concern in operating the photodetector with low power and the photocurrent value would be limited by the unfavorable charge injection from the metal contact. This problem can be overcome by lowering the Schottky barrier via doping. For 2D materials, molecular doping has become the most viable approach to tune the Fermi level of semiconducting materials thanks to the large surface-to-volume ratio for physi(chemi)sorption.[27–30] Instead of employing the most common doping strategies of 2D materials based on aromatic molecules, we have focused our attention to a well-established surfactant molecule, didodecyldimethylammonium bromide (DDAB), containing ionic moiety that can effectively interact with the surface of InSe. Transfer curves of InSe FET were measured after spin-coating the solution in TCE from 10^{-6} to 1 g L^{-1} concentrations. Figure 1d shows that the threshold voltage (V_{th}) shifts negatively with increasing concentrations (output curve changes displayed in Figure S1b and Figure S1c, Supporting Information). The maximum ΔV_{th} obtained within 25 devices with the highest concentration amounts to 42.58 V, corresponding to 1.7×10^{12} cm^{-2} of charge carrier density change. We exclude possible doping from the solvent after thermal annealing, which is ruled out by means of the control experiment reported in Figure S2, Supporting Information.

For 2D materials, molecular doping has become the most viable approach to tune the Fermi level of semiconducting materials thanks to the large surface-to-volume ratio, high chemical reactivity, and sensitivity. The choice of molecules from the huge library of molecules to functionalize with specific 2D material is crucial.[30,31] Fermi level shift in 2D materials could be monitored by Kelvin probe force microscopy (KPFM): Figure 1e shows the surface potential image of a 5.5 nm thick InSe flake before and after its functionalization with DDAB. The profile in Figure 1f reveals that the molecular functionalization determines an increase in surface potential of 200 meV. The resulting work function φ obtained in InSe flake region calibrated with respect to $\varphi_{Pt/Ir}$ shows a decrease from 4.9 to 4.7 eV, indicating the Fermi level lifting towards the conduction band of InSe (Figure S3, Supporting Information). Furthermore, Figure 1e provides evidence for a uniform magnitude in surface potential across the flake, denoting a homogeneous modulation of electronic properties of InSe upon DDAB functionalization.

To fully interpret the origin of such strong doping induced by simple ionic surfactants such as DDAB, Density Functional Theory (DFT) calculations were performed to model the hybrid InSe/DDAB system. Since defects (e.g., Se vacancies) could be generated both during the synthesis of InSe crystal and the delamination by mechanical exfoliation, we considered InSe single layers in either the pristine form (dubbed "InSe" in the following) or including 3% Se vacancies (InSe-3%SeV) (Figure S4, Supporting Information). We explored two molecular conformations for adsorption, with conformation 1 (denoted as InSe (–3%SeV)/DDAB-1) and conformation 2 (denoted as InSe (–3%SeV)/DDAB-2) corresponding to the Br ion being far and close to the InSe surface, respectively (Figure 1g and Figures S5–S8, Supporting Information). The resulting calculated work functions are listed in Figure 1h. We find that functionalization with DDAB molecules determines a work function decrease by 0.09 eV (pristine InSe) and 0.13 eV (defective InSe) in conformation 1, while the corresponding values in conformation 2 are 0.43 eV (pristine InSe) and 0.53 eV (defective InSe). The shifts in work function calculated for the two conformations are in line with the experimental values and result from the combined effect of a partial charge transfer from the molecule to the surface (n-doping) together with a dipolar contribution (of obviously opposite signs in the two conformations considered). Furthermore, we have also observed a systematic improvement of field-effect mobility up to 2785 cm^2 V^{-1} s^{-1} upon the DDAB functionalization, which is due to the combined effect of molecular encapsulation and lowering of contact resistance, as detailed in Supporting Note 2, Supporting Information.[32]

Alongside the DDAB effect on the electrical properties of InSe, we also observed major changes in the optical properties. While Raman modes of InSe have not revealed major changes upon functionalization with DDAB, indicating that the molecular functionalization does not modify the crystal structure of the 2D material, a strong quenching and a 0.8 eV redshift in the photoluminescence (PL) spectra have been monitored (Figure S12, Supporting Information). The variations in PL are in line with previous observations in other n-type 2D materials, such as MoS_2.[33]

4. Molecular Functionalized InSe Field-Effect Phototransistor (photoFET)

Phototransistors are one of the most investigated device structures for 2D photodetectors. Their architectures are identical to bottom-gate top-contact FET, as displayed in Figure 1b. **Figure 2**a–c shows the gate-dependent photoresponse of InSe on SiO_2, BCB, and InSe/DDAB on BCB. A prominent selective photodetection of UV light (365 nm) is observed for both InSe on SiO_2 and BCB. For phototransistor on SiO_2, even at a highly gated region, the measured photocurrent is only in sub-microampere scale with I_{on}/I_{off} around 10^3. The modification of the dielectric layer with BCB leads to an efficient suppression of the undesired recombination from charge traps located at InSe/dielectric interface, thus enhancing the I_{on}/I_{off} ratio up to 10^6 (Figure 2b). The photoresponse rise /decay time has also significantly shortened from 288/447 ms on SiO_2 to 17.33/16.76 ms on BCB. Nevertheless, the photoresponse is still limited by the existence of Se vacancies which could act as traps for photo-generated charge carriers. To minimize such effect, we functionalized the InSe channel with DDAB, by exploiting

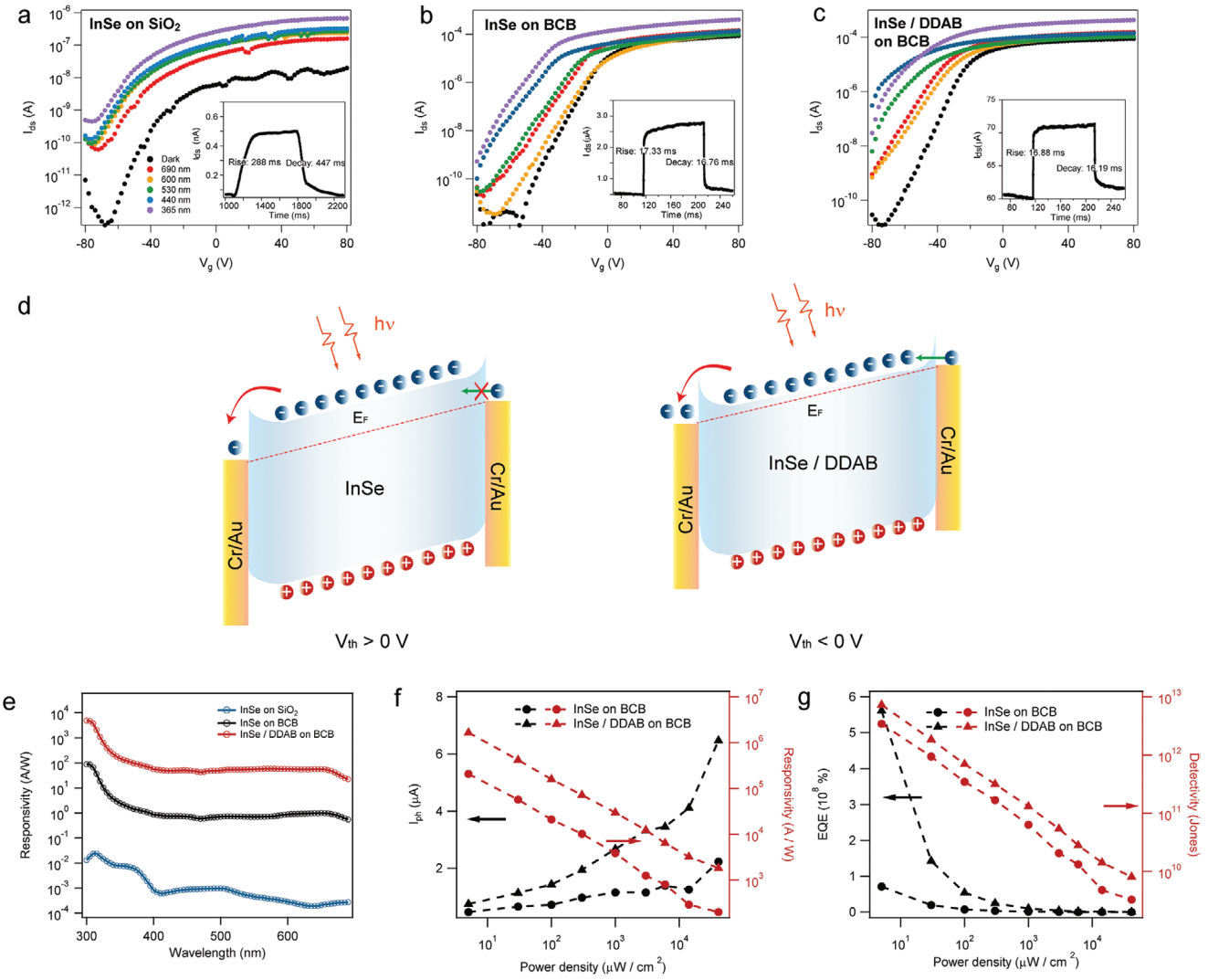

Figure 2. Photoresponsive measurements of photoFET. a–c) I_{ds}-V_g curve of (a) InSe on SiO_2, (b) InSe on BCB, and (c) InSe/DDAB on BCB at $V_g = 0$V and $V_{ds} = 1$V. Inset: time-resolved photoresponse under the illumination of 365 nm at 34.3 mW cm^{-2}. d) Band diagram of InSe photoFET before and after functionalization with DDAB at $V_g = 0$V. The power density is adjusted to 34.3 mW cm^{-2}. e) Calculated responsivity with of wavelength scan from 300 nm to 690 nm at high incident light power (34.3 mW cm^{-2} for 365 nm light). The interval of wavelength is 5 nm. f,g) Power dependence of (f) photocurrent and responsivity and (g) EQE and detectivity of InSe on SiO_2, InSe on BCB, and InSe/DDAB on BCB at $V_g = 0$V and $V_{ds} = 1$V illuminated with 365 nm light.

the propensity of the latter compound to stably adsorb on the Se vacancy sites. The healing of Se vacancies by DDAB could help to restore the crystal structure thereby suppressing the recombination of the photo-generated charges in vacancy traps. Figure 2c provides distinct evidence that such functionalization yields a higher photoresponse. Such enhancement can be ascribed not only to the contribution of Se vacancy healing, but also to the molecular doping induced shift of the V_{th} in InSe FET drawing the device to ON state at $V_g = 0$V which would otherwise be realized by applying a large electrical gate up to 80V.[1,8,13,34] Therefore, with zero contribution from the gate bias, the barrier from the contact is low enough for the photocurrent to tunnel through effectively (Figure 2d). Combining these two factors, we have obtained a reasonably high photocurrent of 12 μA by simply applying 1V of bias voltage in total. The device performance is proved to be stable within light pulse cycles and reproducible among different devices (Figures S13, S14, S29, Supporting Information).

Responsivity (R) of incident wavelength λ is a key parameter to evaluate photocurrent generation of photodetectors. The spectral photoresponse of incident light from 300 to 690 nm for InSe on SiO_2, InSe on BCB, and InSe/DDAB in Figure 2e reveals a single photodetective band from 300 to 400 nm. An exponential enhancement of 10^6 from SiO_2 to BCB as a dielectric is observed. Upon functionalization with DDAB, R reaches 10^5 A W^{-1} (Figure S15d, Supporting Information). Figure 2f,g portrays the photoresponsive characteristics with respect to incident light power intensity (P) of 365 nm for InSe and InSe/DDAB. The photocurrent was found to scale linearity with light power density, complying $I_{ph} \propto P^{\alpha}$. The linearity factor α is calculated to be 0.448 for InSe and 0.658 for InSe/DDAB, implying a reduction of traps.[35] The time-dependent photoresponse at

variable power density is displayed in Figure S16, Supporting Information. EQE represents the efficiency of charge carriers collected per single absorbed photon. In pristine InSe devices, the R and EQE in the low power region (5 μW cm^{-2}) have reached values of 2×10^5 A W^{-1} and 7×10^7%, respectively, indicating an ultra-sensitive photodetection for low-power light. The DDAB functionalization enhances R up to 1×10^6A W^{-1} and EQE to 5×10^8%. Moreover, the photoconductive gain (G), which aid to understand the photogating effect, is evaluated with details reported in Supporting Note 3, Supporting Information. Finally, *D** quantifies the signal-to-noise ratio of a given photodetection area. Power dependent detectivity of InSe and InSe/DDAB is plotted in Figure 2g ranging from 10^9 to 10^{12} for InSe. After functionalization with DDAB, the highest detectivity values reach ≈10^{13} Jones for 5 μW irradiations. Overall, compared to previously reported 2D photodetectors, our molecularly functionalized phototransistors operating with ultra-low voltages (V_g = 0V, V_{ds} = 1V) have displayed extremely high responsivity up to 10^6 A W^{-1}, EQE approaching 10^8%, and detectivity of 10^{13} Jones in the 300 to 690 nm wavelength region. It also exhibits ultra-fast time response for low-power (50μW cm^{-2}, Figure S17, Supporting Information) illumination reaching a response time of 4.9 ms.

5. Molecular Functionalized InSe Asymmetric Schottky Junction

Photodetectors based on 2D lateral p-n junctions have been realized by either controlling the semiconducting channel region by selective doping, or by manipulating the electron/hole injection through the use of asymmetric metal contact.[22,36–40] Here we adopt both strategies to realize high-performance lateral p-n junction based on multi-layer InSe by chemical doping with DDAB. The device structure is shown in **Figure 3**a. We have carefully chosen metals with high and low work functions (Pd: ≈5.6 eV Cr: 4.4 eV) to form a large Schottky barrier difference.[41–43] The metal-semiconductor contact is analyzed in Figure S18, Supporting Information, revealing a large Schottky barrier with Pd and a smaller Schottky barrier on Cr. Therefore, a depletion region is formed at the Pd-InSe interface thereby p-doping the contact region of InSe (Figure 3b). While the n-doping by DDAB is uniform for InSe, the hole transport region is protected by a few-layer of hexagonal boron nitride (h-BN) as displayed in the Atomic Force Microscopy (AFM) image in Figure 3c. The device showed a gate-dependent rectification where the rectification ratio amounts to 198 at V_g = 0V in dark (Figure 3d). After doping with DDAB, the reverse bias current maintained in sub-nanoampere range with a fivefold increase in the forward bias current, reaching a rectification ratio of 716. The obtained functionalized Schottky junction exhibits an ideal factor η around 1, rendering it an ideal diode (Supporting Note 4, Supporting Information). The wavelength-dependent photodetective properties of such a p-n junction are evaluated in Figure 3e,f. Similar to InSe phototransistor, the lateral p-n junction shows selective photoresponse for UV light (Figure S20, Supporting Information). Additional photodetection test on 850 and 940 nm near-infrared (NIR) light is presented in Figure S21, Supporting Information. The device displays strong power dependence (Figure 3g–i and Figure S22, Supporting Information). The linearity factor drops from 0.8440 for InSe/h-BN to 0.8065 for InSe/h-BN/DDAB, likely because of the inhomogeneity in the channel where the n-region is governed by the physisorbed organic molecules, while the p-region is screened by crystalline inorganic h-BN. Furthermore, by calculating R, EQE, and D*, the lateral P-N junction reaches high R and EQE exceeding 10^3 A W^{-1} and 3×10^5% upon 5 μW cm^{-2} illumination after DDAB functionalization, being 4 times greater than undoped junction. Simultaneously, *D** also shows tenfold enhancement at low power illumination, reaching 4×10^{11} Jones. The photoresponse time of the lateral P-N junction is also found to be ultrafast for both unfunctionalized and functionalized samples, which all decreased below 1 ms (Figure S23, Supporting Information). Compared to previously reported InSe lateral P-N junctions, our molecular functionalized device not only represents a novel device architecture that is highly suitable for exploring the photodetection of InSe, but also displayed record performance when operating at very low voltage inputs, demonstrating the power of molecular doping in InSe Schottky junctions.

6. Molecular Functionalized BP-InSe Van der Waals p-n Heterostructures

2D materials have been widely exploited as building blocks for vdW p-n heterostructures with tunable bandgaps by varying the material composition and thicknesses. As an n-type semiconducting material, InSe could form type-II band alignment with various p-type 2D semiconductors including the archetypical natural p-doped 2D material is black phosphorus (BP), which possesses a small bandgap of ≈ 0.3 eV. The band alignment of BP and InSe is demonstrated in Figure S24, Supporting Information. While the development of functional devices based on BP heterostructures with graphene, MoS_2, ReS_2, etc. have been widely reported in the literature, only two recent papers reported BP-based heterostructure with InSe which unfortunately did not demonstrate reliable high-performance photodetectors as other 2D materials.[44–48] This is achieved here, where we first focus on the dielectric engineering of the BP-InSe heterostructure showing evident performance enhancement of the P-N junction, as discussed in detail in Supporting Note 5 and Figures S25 and S26, Supporting Information.

Based on previous discussions, electron doping in the n-region is beneficial for enhancing the performances of P-N junctions. Therefore, it is reasonable to envisage a strong molecular n-dopant such as DDAB could easily promote the photodetection properties. In order to isolate BP from molecular doping, we partially passivated the BP flake with h-BN to prevent its exposure to molecules, as displayed in **Figure 4**a. After functionalization with DDAB, a nearly tenfold increase in the forward bias photocurrent has been recorded, while the reverse bias current retained the same magnitude (Figure 4b,c, Figure S27, Supporting Information). Such observations can be explained by the upshift of Fermi level in the n-InSe region, prompting a larger built-in potential in the depletion region. This allows photoinduced excitons to easily dissociate into photoelectrons (holes) across the heterostructure, assisted by

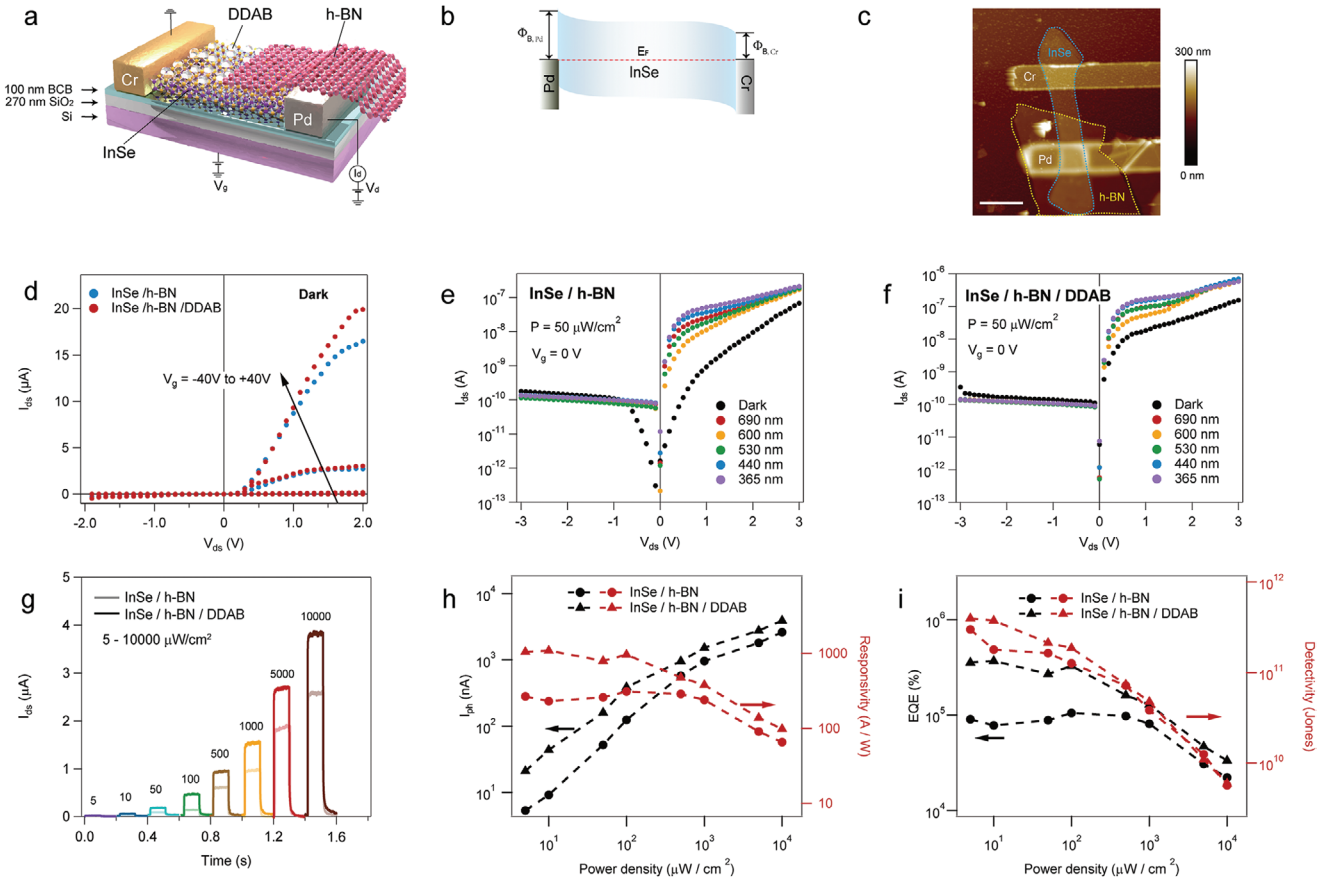

Figure 3. Molecular functionalization of lateral InSe asymmetric Schottky junction. a) Illustration of the device structure of lateral InSe asymmetric Schottky junction. b) Band alignment of InSe with Pd and Cr contacts. Here, the Schottky barrier height (SBH) was estimated from Ref. [43] where the SBH is 280 and 560 meV for Cr and Pd respectively. c) AFM image of representative lateral InSe asymmetric Schottky junction partially covered with few-layer h-BN on top. The scale bar is 6 μm. d) Gate-dependent I-V curves of InSe/h-BN before and after doping with DDAB in dark conditions. e) Photodetection of lateral InSe asymmetric Schottky junction before doping with DDAB. f) Photodetection of lateral InSe asymmetric Schottky junction after doping with DDAB. The weak photoresponse at reverse bias indicates a back-to-back connected diode with only one side illuminated due to the presence of Schottky barriers at both contacts. g) Time-dependent photoresponse of power density ranging from 5 to 5000μW cm^{-2} of InSe/h-BN and InSe/h-BN/DDAB. h,i) Power dependence of (h) photocurrent and responsivity and (i) EQE and D^* of InSe/h-BN InSe/h-BN/DDAB on BCB at V_g = 0V and V_d = 1V illuminated with 365 nm light.

an external drain bias of 1V. In this regard, the photoresponse time has also drastically decreased from 24.40/36.41 ms to 0.96/2.97 ms, which could be ascribed to drifting of photocarriers (electrons to n-InSe and holes to p-BP) facilitated by the larger potential difference at the vdW interface as well as the molecular functionalization filling the defect states of InSe, thereby reducing the scattering of photocarriers that would notably slow down the photoresponse time (Figure 4d,e). The enhancement of the functionalization is proved to be reproducible in different devices (Figure S28, Supporting Information). Compared to pure InSe with single absorption band (Figure 4f), the spectral R of the heterostructure showed two additional absorption bands from 450 to 550 nm and from 600 to 690 nm. It is attributed to the presence of BP who possesses a much smaller bandgap, is able to generate larger photocurrent at the large wavelength region compared to pure InSe, contributing to the total photocurrent response, which is reflected as additional photocurrent absorption bands in the spectrum. The R value reaches a maximum value of 46 and 537 A W^{-1} at 365 nm before and after the molecular functionalization, respectively. The ultrahigh responsivity reaches a record value among reported 2D-2D P-N heterostructures, especially, by operating the device with only 1V of voltage input. The power-dependent photodetection from 5 to 4120 μW cm^{-2} before and after the DDAB doping in Figure 4g–i indicates the photocurrent improvement to be universal for different power densities. By calculating the linearity factor, we obtain $\alpha = 0.44$ for non-functionalized and $\alpha = 0.48$ for functionalized heterostructure, revealing a reduction of the amount of impurities (e.g., defects) in the P-N junction. The highest R and EQE exceeded 10^3 A W^{-1} and 3.5×10^5% after the functionalization, being almost 2 orders of magnitude larger than the unfunctionalized device while D^* remains on the same range of 10^{11} Jones. The successful realization of vdW BP-InSe P-N heterostructure and its performance improvement provides even stronger evidence of the high relevance of molecular functionalization of InSe to boost performances in a broad range of opto-electronic device types, and in particular for low-power ultra-responsive photodetectors.

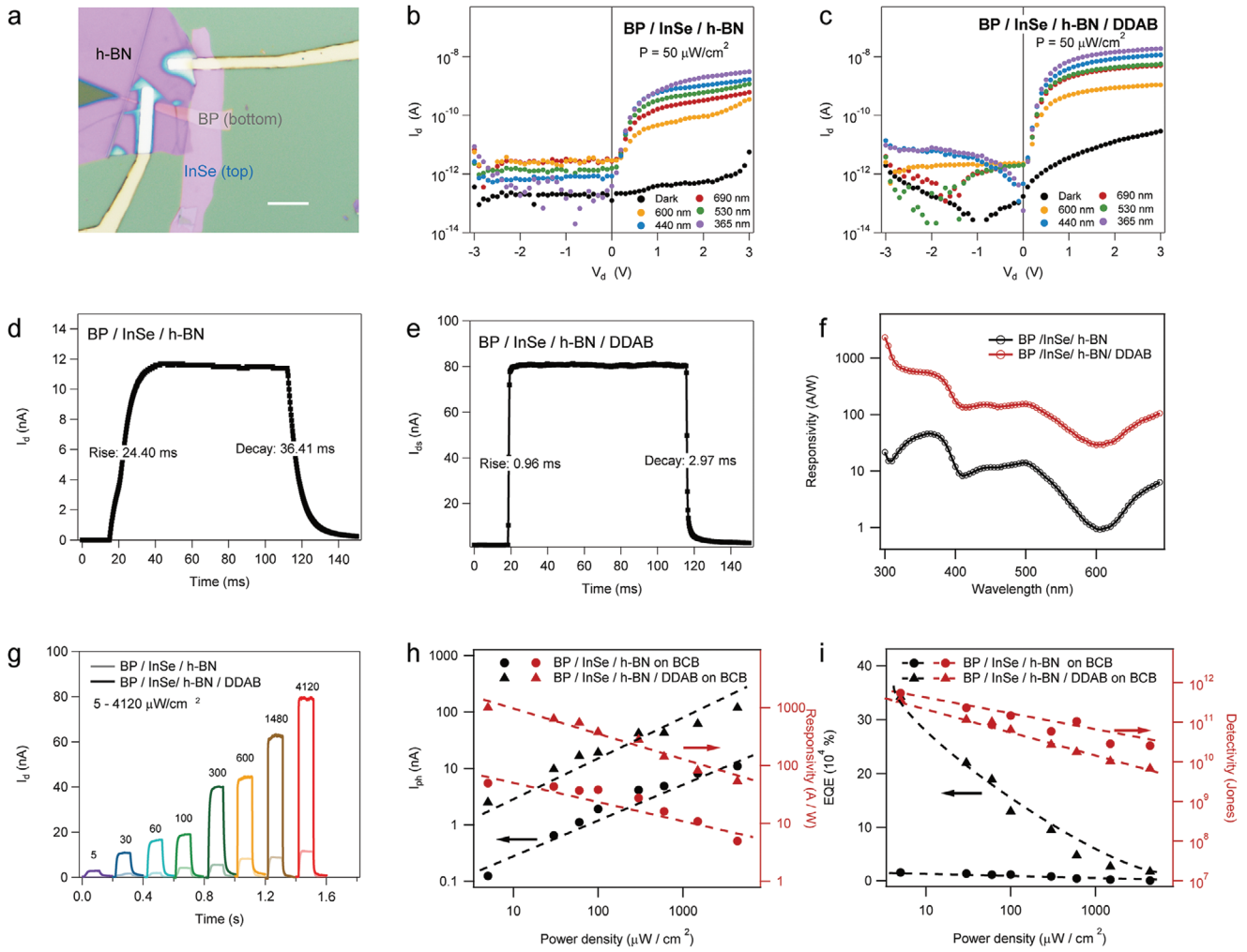

Figure 4. Molecular functionalization of BP-InSe P-N junctions. a) Optical image of BP/InSe heterostructure partially encapsulated by h-BN. The scale bar is 10 μm. b,c) Output curves of BP/InSe/h-BN heterostructure (b) before and (c) after the functionalization of DDAB. On BCB substrate, due to the enhanced n-type transport also in BP (as it is ambipolar under Cr contact), we have observed larger photoresponse at forward bias than reverse bias. d,e) Time-resolved photoresponse of (d) BP/ InSe/ h-BN and (e) BP/ InSe/ h-BN/ DDAB at $V_g = 0$V and $V_d = 1$V under the illumination of 365 nm. Light power is adjusted at 4.12 mW cm^{-2}. f) Spectral responsivity of wavelength scan from 300 to 690 nm at $V_g = 0$V and $V_{ds} = 1$V. The interval of wavelength is 5 nm. g) Photoresponse of power density ranging from 5 to 4120 μW cm^{-2} of BP/ InSe/h-BN and BP/ InSe/h-BN/DDAB. h,i) Power dependence of (h) photocurrent and responsivity and (i) EQE and D^* of BP/InSe/h-BN and InSe/h-BN/DDAB at $V_g = 0$ V and $V_d = 1$V illuminated with 365 nm light.

7. Conclusions

In summary, we have demonstrated novel strategies for markedly improving the performances of multifunctional opto-electronic devices based on a few-layer InSe by means of dielectric engineering using trap-free polymer and molecular functionalization with DDAB. By combining experimental work with theoretical calculations, we showed that DDAB could form a stable physisorbed layer onto the surface of InSe by lowering the Fermi level and, at the same time, healing the defect states of InSe. The resulting transistors displayed field-effect mobilities exceeding 10^3 cm^2 V^{-1} s^{-1} with a high doping density of 10^{12} cm^{-2}. By further exploring molecular functionalized InSe as photodetectors, we successfully fabricated InSe devices in the form of phototransistor, Schottky contact lateral P-N junction, and vdW vertical P-N junction with ultra-high performances even when operated at very low bias input. The phototransistor reaches ultra-high photoresponsivity of 10^6 A W^{-1}, meanwhile showing very fast photoresponse below 5 ms. The photoresponse time was efficiently decreased to sub-microsecond scale with molecular doped P-N junction, meanwhile, the EQE was enhanced up to 10^5%, thus outperforming previous reports of 2D P-N junctions (Supporting Table 2 in Supporting Information). The high photoresponsivity is reproducible among devices (Figure S29, Supporting Information). This work provides distinct evidence of the full potential of molecular doping of InSe as a viable platform for improving the functional complexity and ultimately fabricates a high-performance 2D opto-electronic device. More generally, the employed chemical functionalization does not require sophisticated instruments; it is efficient, practical, up-scalable, and widely applicable to manipulate at will various physical properties of 2D semiconductors for large-area applications.

8. Experimental Section

Sample Preparation: BCB dielectric was prepared by diluting Cyclotene 3022–46 (Dow Chemistry) to 20%vol with mesitylene. The solution was spin-coated onto thermally oxidized heavily *n*-doped silicon substrates (Fraunhofer Institute IPMS, $\rho_{Si} \approx 0.001\ \Omega$ cm, $t_{ox} = 270$ nm) at 4000RPM and post-anneal at 290 °C resulting in film thickness of 100 nm. It was noticed that a lower concentration of BCB solution or higher rotation speed for spin-coating sometimes results in inhomogeneous films and thicker BCB film (>100 nm) would require a higher gate voltage range for manipulation because of the lowering of the capacitance of the total dielectric. For InSe phototransistors and asymmetric Schottky junctions, few-layer InSe (10–15 nm thick) were mechanically exfoliated from commercially available InSe crystals (HQ Graphene, Netherland) using the scotch tape method and transferred on SiO_2 or BCB in an N_2-filled glovebox. Their thickness was monitored by optical microscope combined with Raman spectroscopy and AFM. For BP-InSe heterostructures, few-layer BP flakes (5–10 nm thick) were first mechanically exfoliated onto BCB substrate in glovebox. Few-layer InSe (10–20 nm thick) were immediately transferred onto BP by PDMS to form vdW heterostructure. The samples were thermally annealed at 100 °C inside a vacuum chamber to desorb atmospheric adsorbates and to reinforce the vdW contact. For molecular functionalization, DDAB solution (Tokyo Chemical Industry Co., Ltd (TCI)) with 10^{-6}, 10^{-5}, 10^{-4}, 10^{-3}, 10^{-2}, 10^{-1}, and 1 g L^{-1} of concentration were spin-coated at 2000 RPM onto InSe. A post thermal annealing at 120 °C was applied on the hotplate in an N_2-filled glovebox.

Device Fabrication: InSe devices were patterned by photolithography (AZ1505 photoresist and MIF726 developer, Micro Chemicals) using laser writer LW405B from Microtech. InSe photoFET and BP/InSe P-N photodetector were thermally evaporated with Plassys MEB 300 following a lift-off process in warm acetone to obtain the final source and drain electrodes. For asymmetric Schottky junctions, one electrode was first patterned with laser writer and 60 nm Pd was deposited with Egun evaporator Plassys ME300, after lift-off in warm acetone, a second electrode was patterned followed by thermal deposition of 5 nm chromium and 40 nm of gold by Plassys MEB300B equipped in the glovebox. The devices were rinsed with acetone and 2-propanol to remove resist residues. All devices were annealed under vacuum at 100 °C to remove absorbents.

Electrical Characterizations: The characterization of device performance was realized by Keithley 2636A under N_2 atmosphere. For optoelectronic characterizations, a Polychrome V system (Thermo Fisher) was used as a monochromatic light source. The output power has been calibrated by a PM100A Power Meter (Thorlabs). The detailed calculation of optoelectronic parameters could be found in Supporting Note S1, Supporting Information.

Raman Spectroscopy: Raman and Photoluminescence spectra were carried out in an inert atmosphere (N_2) by Renishaw inVia spectrometer equipped with 532 nm laser in a nitrogen-filled sealed holder (Linkam). Samples were mounted in the glovebox and immediately measured after annealing or after molecule deposition to avoid exposure to contaminant chemicals. The excitation power was kept below 1 mW to avoid local heating damage effects. The wavenumber (energy) resolution was ≈1 meV.

AFM Measurement: AFM imaging was performed by means of a Bruker Dimension Icon set-up operating in air, in tapping mode, by using tip model TESPA-V2 (tip stiffness: k = 42 N m^{-1}).

KPFM Measurement: A Bruker Icon AFM was employed for KPFM experiments. Topography and surface potential (or contact potential difference) images were simultaneously collected with Pt/Ir coated silicon probes (Bruker SCM-PIT-V2, resonant frequency ≈ 75 kHz, k ≈ 3 N m^{-1}) at ambient conditions in the amplitude modulation mode. Macroscopic Kelvin Probe (KP) measurements were performed by using a 2-mm-diameter gold tip amplifier (Ambient Kelvin Probe Package from KP Technology Ltd) at ambient conditions. The calibration of the probe was performed against a freshly cleaved HOPG surface (4.475 eV).[49]

XPS Measurements: XPS analyses were carried out with a Thermo Scientific K-Alpha X-ray photoelectron spectrometer with a basic chamber pressure of ≈10^{-9} mbar and an Al anode as the X-ray source (X-ray radiation of 1486 eV). Spot sizes of 400 µm and pass energies of 200.00 eV for wide energy scans and 10.00–20.00 eV for scans were used.

Computational Details: All DFT calculations were performed using the VASP code[50] and the projector-augmented wave (PAW) basis set. Exchange and correlation effects were treated at the Perdew–Burke–Ernzerhof (PBE) level with the dispersion forces treated by Grimme correction (PBE+D2), with a kinetic energy cut-off of 500 eV and using a Monkhorst-Pack sampling of 3 × 3 × 1 for the Brillouin zone (BZ) integration on the unit cell replicated 4 × 4 × 1 times with the vacuum spacing set to be 40 Å to avoid the interaction with periodic images.[51–54] One Se atom was removed from InSe unit-cell replicated to 4 × 4 × 1 super-cell, generating an optimal vacancy concentration of ≈ 3%, in line with previous investigations.[55–57] Dipole moment correction was employed along the "c" axis (Z direction & perpendicular to the InSe surface). Geometries of pristine and defective (–3% Se vacancies) InSe surfaces, as well as the DDAB adsorbed heterostructures, were fully optimized at the PBE/GGA level of theory prior to the calculation of work function. DDAB molecules were considered with two butyl (C_4) linkers (dibutyl-dimethyl-ammonium, bromide) instead of two decyl (C_{10}) linkers connecting the central nitrogen atom, so as to limit the computational cost. The work function (ϕ) of all the systems was calculated as the difference of Fermi energy (E_f, taken as the middle of the bandgap) and the electrostatic potential at vacuum level (E_p) at the hybrid (HSE06) level of theory.

Supporting Information

Supporting Information is available from the Wiley Online Library or from the author.

Acknowledgements

The authors thank Dr. Yuda Zhao (Zhejiang University, China) and Dr. Chun Ma (University of Strasbourg, France) for fruitful discussions. The authors acknowledge funding from European Commission through the ERC project SUPRA2DMAT (GA-833707), the Graphene Flagship Core 3 project (GA- 881603) and the Marie Curie ITN project UHMob (GA-811284), the Agence Nationale de la Recherche through the Labex projects CSC (ANR-10-LABX-0026 CSC), and NIE (ANR-11-LABX-0058 NIE) within the Investissement d'Avenir program (ANR-10-120 IDEX-0002-02), the International Center for Frontier Research in Chemistry (icFRC). The work in Mons was supported by the Belgian National Fund for Scientific Research (FRS-FNRS), within FNRS-PDR-TOREADOR project. Computational resources were provided by the Consortium des Équipements de Calcul Intensif (CÉCI) funded by F.R.S.-FNRS under Grant 2.5020.11. D.B. is FNRS Research Director.

Conflict of Interest

The authors declare no conflict of interest.

Author Information

P.S., Y.W., and H.W. conceived and coordinated the work. Y.W. worked on sample preparation, device fabrication, optical, and electrical characterization. H.W. worked on the molecule selection and preparation. S.M.G. did the modeling work, under the supervision of D.B. N.T. performed the KPFM. Y.W. measured the AFM with C.W. Y.Y. and Y.W. established the optoelectronic measurement setup. Y.C. participated in metal evaporation. Y.W. analyzed the data. Y.W. and P.S. wrote the paper with all the authors contributing to the discussion and preparation of the manuscript. Correspondence and requests for materials should be addressed to P.S.

Data Availability Statement

Data available on request from the authors.

Keywords

2D material, black phosphorus, doping, indium selenide, photodetectors, p-n junctions, van der Waals heterostructures

Received: April 10, 2021
Published online:

[1] M. Long, P. Wang, H. Fang, W. Hu, *Adv. Funct. Mater.* **2019**, *29*, 1803807.
[2] L. Sang, M. Liao, M. Sumiya, *Sensors* **2013**, *13*, 10482.
[3] D. Natali, M. Caironi, in *Photodetectors*, Elsevier, Woodhead Publishing, Cambridge **2016**, p. 195.
[4] Y. L. Wu, K. Fukuda, T. Yokota, T. Someya, *Adv. Mater.* **2019**, *31*, 1903687.
[5] Z. Chen, J. Biscaras, A. Shukla, *Nanoscale* **2015**, *7*, 5981.
[6] M. Li, C. Y. Lin, S. H. Yang, Y. M. Chang, J. K. Chang, F. S. Yang, C. Zhong, W. B. Jian, C. H. Lien, C. H. Ho, *Adv. Mater.* **2018**, *30*, 1803690.
[7] Y. Yang, J. Jeon, J.-H. Park, M. S. Jeong, B. H. Lee, E. Hwang, S. Lee, *ACS Nano* **2019**, *13*, 8804.
[8] W. Feng, J.-B. Wu, X. Li, W. Zheng, X. Zhou, K. Xiao, W. Cao, B. Yang, J.-C. Idrobo, L. Basile, *J. Mater. Chem. C* **2015**, *3*, 7022.
[9] M. Long, E. Liu, P. Wang, A. Gao, H. Xia, W. Luo, B. Wang, J. Zeng, Y. Fu, K. Xu, *Nano Lett.* **2016**, *16*, 2254.
[10] J. Heo, H. Jeong, Y. Cho, J. Lee, K. Lee, S. Nam, E.-K. Lee, S. Lee, H. Lee, S. Hwang, *Nano Lett.* **2016**, *16*, 6746.
[11] Q. Lv, F. Yan, X. Wei, K. Wang, *Adv. Opt. Mater.* **2018**, *6*, 1700490.
[12] X. Zhou, X. Hu, B. Jin, J. Yu, K. Liu, H. Li, T. Zhai, *Adv. Sci.* **2018**, *5*, 1800478.
[13] O. Lopez-Sanchez, D. Lembke, M. Kayci, A. Radenovic, A. Kis, *Nat. Nanotechnol.* **2013**, *8*, 497.
[14] D. A. Nguyen, H. M. Oh, N. T. Duong, S. Bang, S. J. Yoon, M. S. Jeong, *ACS Appl. Mater. Interfaces* **2018**, *10*, 10322.
[15] W. Zhang, M.-H. Chiu, C.-H. Chen, W. Chen, L.-J. Li, A. T. S. Wee, *ACS Nano* **2014**, *8*, 8653.
[16] S. R. Tamalampudi, Y.-Y. Lu, R. K. U, R. Sankar, C.-D. Liao, C.-H. Cheng, F. C. Chou, Y.-T. Chen, *Nano Lett.* **2014**, *14*, 2800.
[17] D. A. Bandurin, A. V. Tyurnina, L. Y. Geliang, A. Mishchenko, V. Zólyomi, S. V. Morozov, R. K. Kumar, R. V. Gorbachev, Z. R. Kudrynskyi, S. Pezzini, *Nat. Nanotechnol.* **2017**, *12*, 223.
[18] M. Gobbi, E. Orgiu, P. Samorì, *Adv. Mater.* **2018**, *30*, 1706103.
[19] S. Bertolazzi, M. Gobbi, Y. Zhao, C. Backes, P. Samorì, *Chem. Soc. Rev.* **2018**, *47*, 6845.
[20] B. Chamlagain, Q. Li, N. J. Ghimire, H. J. Chuang, M. M. Perera, H. Tu, Y. Xu, M. Pan, D. Xaio, J. Yan, D. Mandrus, Z. Zhou, *ACS Nano* **2014**, *8*, 5079.
[21] K. Dolui, I. Rungger, S. Sanvito, *Phys. Rev. B* **2013**, *87*, 165402.
[22] Y. Zhao, S. Bertolazzi, P. Samorì, *ACS Nano* **2019**, *13*, 4814.
[23] Z. Yu, Z. Y. Ong, S. Li, J. B. Xu, G. Zhang, Y. W. Zhang, Y. Shi, X. Wang, *Adv. Funct. Mater.* **2017**, *27*, 1604093.
[24] A. H. Edwards, in *The Physics and Chemistry of SiO_2 and the Si-SiO_2 Interface*, Springer US, New York **1988**, p. 271.
[25] E. H. Poindexter, P. J. Caplan, G. J. Gerardi, in *The Physics and Chemistry of SiO_2 and the Si-SiO_2 Interface*, Springer US, New York **1988**, p. 299.
[26] Y. Guo, X. Wei, J. Shu, B. Liu, J. Yin, C. Guan, Y. Han, S. Gao, Q. Chen, *Appl. Phys. Lett.* **2015**, *106*, 103109.
[27] X. Dong, D. Fu, W. Fang, Y. Shi, P. Chen, L. J. Li, *Small* **2009**, *5*, 1422.
[28] Y. C. Du, H. Liu, A. T. Neal, M. W. Si, P. D. Ye, *IEEE Electron Device Lett.* **2013**, *34*, 1328.
[29] M.-A. Stoeckel, M. Gobbi, T. Leydecker, Y. Wang, M. Eredia, S. Bonacchi, R. Verucchi, M. Timpel, M. V. Nardi, E. Orgiu, P. Samorì, *ACS Nano* **2019**, *13*, 11613.
[30] Y. Wang, A. Slassi, M.-A. Stoeckel, S. Bertolazzi, J. Cornil, D. Beljonne, P. Samorì, *J. Phys. Chem. Lett.* **2019**, *10*, 540.
[31] Y. Wang, S. M. Gali, A. Slassi, D. Beljonne, P. Samorì, *Adv. Funct. Mater.* **2020**, *30*, 2002846.
[32] J. Sun, Y. Wang, S. Guo, B. Wan, L. Dong, Y. Gu, C. Song, C. Pan, Q. Zhang, L. Gu, *Adv. Mater.* **2020**, *32*, 1906499.
[33] S. Mouri, Y. Miyauchi, K. Matsuda, *Nano Lett.* **2013**, *13*, 5944.
[34] W. Luo, Y. Cao, P. Hu, K. Cai, Q. Feng, F. Yan, T. Yan, X. Zhang, K. Wang, *Adv. Opt. Mater.* **2015**, *3*, 1418.
[35] Q. Zhao, W. Wang, F. Carrascoso-Plana, W. Jie, T. Wang, A. Castellanos-Gomez, R. Frisenda, *Mater. Horiz.* **2020**, *7*, 252.
[36] M. S. Choi, D. Qu, D. Lee, X. Liu, K. Watanabe, T. Taniguchi, W. J. Yoo, *ACS Nano* **2014**, *8*, 9332.
[37] J. S. Ross, P. Klement, A. M. Jones, N. J. Ghimire, J. Yan, D. Mandrus, T. Taniguchi, K. Watanabe, K. Kitamura, W. Yao, *Nat. Nanotechnol.* **2014**, *9*, 268.
[38] M. Dai, H. Chen, F. Wang, M. Long, H. Shang, Y. Hu, W. Li, C. Ge, J. Zhang, T. Zhai, *ACS Nano* **2020**, *14*, 9098.
[39] M. Dai, H. Chen, R. Feng, W. Feng, Y. Hu, H. Yang, G. Liu, X. Chen, J. Zhang, C.-Y. Xu, *ACS Nano* **2018**, *12*, 8739.
[40] S. Hu, Q. Zhang, X. Luo, X. Zhang, T. Wang, Y. Cheng, W. Jie, J. Zhao, T. Mei, X. Gan, *Nanoscale* **2020**, *12*, 4094.
[41] D. J. Perello, S. H. Chae, S. Song, Y. H. Lee, *Nat. Commun.* **2015**, *6*, 7809.
[42] C. Kim, I. Moon, D. Lee, M. S. Choi, F. Ahmed, S. Nam, Y. Cho, H.-J. Shin, S. Park, W. J. Yoo, *ACS Nano* **2017**, *11*, 1588.
[43] Y.-H. Chen, C.-Y. Cheng, S.-Y. Chen, J. S. D. Rodriguez, H.-T. Liao, K. Watanabe, T. Taniguchi, C.-W. Chen, R. Sankar, F.-C. Chou, *npj 2D Mater. Appl.* **2019**, *3*, 1.
[44] R. Cao, H. D. Wang, Z. N. Guo, D. K. Sang, L. Y. Zhang, Q. L. Xiao, Y. P. Zhang, D. Y. Fan, J. Q. Li, H. Zhang, *Adv. Opt. Mater.* **2019**, *7*, 1900020.
[45] S. Zhao, J. Wu, K. Jin, H. Ding, T. Li, C. Wu, N. Pan, X. Wang, *Adv. Funct. Mater.* **2018**, *28*, 1802011.
[46] Y. Deng, Z. Luo, N. J. Conrad, H. Liu, Y. Gong, S. Najmaei, P. M. Ajayan, J. Lou, X. Xu, P. D. Ye, *ACS Nano* **2014**, *8*, 8292.
[47] S. Cao, Y. Xing, J. Han, X. Luo, W. Lv, W. Lv, B. Zhang, Z. Zeng, *Nanoscale* **2018**, *10*, 16805.
[48] X. K. Li, X. G. Gao, B. W. Su, W. Xin, K. X. Huang, X. Q. Jiang, Z. B. Liu, J. G. Tian, *Adv. Mater. Interfaces* **2018**, *5*, 1800960.
[49] W. N. Hansen, G. J. Hansen, *Surf. Sci.* **2001**, *481*, 172.
[50] G. Kresse, M. Marsman, J. Furthmüller, *VASP* **2012**.
[51] G. Kresse, J. Furthmüller, *Phys. Rev. B* **1996**, *54*, 11169.
[52] G. Kresse, D. Joubert, *Phys. Rev. B* **1999**, *59*, 1758.
[53] J. P. Perdew, K. Burke, M. Ernzerhof, *Phys. Rev. Lett.* **1996**, *77*, 3865.
[54] S. Grimme, *J. Comput. Chem.* **2006**, *27*, 1787.
[55] D. Chen, X. Zhang, H. Cui, J. Tang, S. Pi, Z. Cui, Y. Li, Y. Zhang, *Appl. Surf. Sci.* **2019**, *479*, 852.
[56] X. Liu, J.-C. Ren, S. Zhang, M. Fuentes-Cabrera, S. Li, W. Liu, *J. Phys. Chem. Lett.* **2018**, *9*, 3897.
[57] B. Ma, Y. Peng, D. Ma, Z. Deng, Z. Lu, *Appl. Surf. Sci.* **2019**, *495*, 143463.